Responses to the comments

We would like to express our gratitude and deep thanks to the reviewers and editors for taking the time to review our work and for their comments which help focus the goal of this research.

The topic is relevant, and the attempt to combine two-phase flow, thermal effects, and DBF momentum balance in one acidizing model is potentially valuable. The manuscript also addresses an important practical issue: how thermal and hydrodynamic conditions influence wormhole formation. However, in its present form, the paper does not yet provide sufficient methodological rigor or numerical evidence to support its claims at the publication level. The most serious issues are the lack of proper verification/validation, insufficient numerical detail, limited quantitative analysis, and several places where the claims are stronger than the presented evidence. For these reasons, I recommend major revision.

Major comments:

1. The manuscript contains a section titled "Verification experiments," but this does not constitute verification in the numerical sense. Instead, it presents an additional parametric study on the effect of injection velocity. It does not validate the solver against analytical solutions, benchmark problems, experimental data, or previously validated numerical results. I recommend adding a proper verification section after the methodology and before the numerical experiments. This section should demonstrate the validity of the model—either as a whole or for its individual components—by comparison with existing benchmarks or, at a minimum, previously published numerical models.

Response: We have added the verification section in the new manuscript.

2. A central weakness of the paper is that the solution procedure is not described with sufficient clarity for reproducibility. The current presentation makes it difficult for readers to understand how the coupled problem is actually solved. This section should explicitly clarify:

- whether the coupling strategy is fully implicit (monolithic), sequential implicit, or loosely coupled. From the current description, it appears that a staggered approach is used, which does not fully enforce coupling between the primary variables;
- whether any inner (within–time step) iterations are performed;

- the convergence criteria adopted;
- how nonlinear residuals are defined and monitored;
- how boundary conditions are imposed for pressure, saturation, concentration, and temperature;
- how stability is influenced by the treatment of thermal source/transport terms (Eq. 8), particularly given the use of explicit discretization, and the rationale for this choice;
- the justification for and implementation of upwind discretization for edge saturations and acid concentration.

I also recommend including the fully discretized form of the governing equations (as it appears a finite difference method is employed), along with a clear flowchart of the solution algorithm, to ensure transparency and reproducibility.

Response: We thank the reviewer for the valuable comments regarding the clarity and reproducibility of the numerical implementation. We agree that the original manuscript did not provide sufficient detail on the coupling strategy and numerical solution procedure. To address this concern, we have substantially revised the "Solution Procedure" section and added additional explanations regarding the discretization and coupling strategy.

First, we now explicitly state that the proposed solver adopts a sequential implicit staggered coupling strategy rather than a fully monolithic formulation. In each time step, the primary variables are updated sequentially in the following order: porosity, saturation, pressure/velocity, acid concentration, and temperature. The coupling between variables is handled through updated coefficients and source terms passed between successive substeps.

Second, we clarify that no inner nonlinear iterations are performed within each time step. Instead, the nonlinear terms are linearized using previously updated variables from the current or previous time level. We also explain the linearization treatment for the nonlinear DBF momentum terms and reactive source terms.

Third, the simulations are advanced using sufficiently small time steps to ensure stable evolution of the coupled thermo-hydraulic-reactive system. The breakthrough criterion and grid-convergence verification are now described more clearly in the revised manuscript.

Fourth, the detailed description of the boundary conditions imposed for pressure, saturation, concentration, and temperature, including the inlet velocity condition, outlet pressure condition, impermeable wall treatment, and thermal boundary assumptions is given in the experiment section.

Fifth, the rationale for the discretization strategy has been clarified. In particular, the advection-dominated saturation and concentration transport terms are discretized using an upwind scheme to suppress nonphysical oscillations and improve numerical stability near steep displacement fronts. The thermal transport equation adopts a partially explicit treatment for several source and transport terms to reduce computational cost and avoid solving a strongly nonlinear fully coupled thermal system within each time step. The stability of this treatment is maintained through the use of sufficiently small time steps.

Finally, following the reviewer's suggestion, we have added a flowchart summarizing the overall numerical algorithm, with the aim of improving transparency and reproducibility of the implementation.

3. The paper states that the model can simulate complex field phenomena "with high fidelity" and bridge the gap to **practical field applications**. This is too strong for a 2D lab-scale numerical demonstration without validation. Similarly, the conclusion section moves quickly toward future field-scale, surrogate-model, and optimization applications, but the present manuscript has not yet demonstrated the reliability required for such extensions. The authors should moderate these claims and more clearly position the work as a methodological step rather than a validated predictive tool.

Response: We thank the reviewer for this important comment. We agree that several statements in the original manuscript overstated the current level of validation and applicability of the proposed model. The present work is primarily intended as a methodological and numerical study for investigating the coupled thermo-hydraulic-reactive behavior in two-phase acidizing systems, rather than as a fully validated predictive field-scale simulator.

Following the reviewer's suggestion, we have revised the manuscript to moderate these claims throughout the Introduction, Results, and Conclusion sections. In particular, phrases such as "with high fidelity" and statements implying direct field-scale predictive capability have been removed or reworded. The revised manuscript now emphasizes that the proposed framework represents a proof-of-concept numerical methodology for studying the influence of thermal and hydrodynamic conditions on dissolution behavior and wormhole formation.

We have also clarified that the current simulations are limited to two-dimensional laboratory-scale numerical experiments and that additional validation against experimental data, benchmark studies, and larger-scale simulations is required before practical field-scale predictive applications can be claimed. Furthermore, discussions related to surrogate modeling, optimization, and field applications are now presented more carefully as possible future research directions rather than demonstrated capabilities of the current study.

4. The discussion relies heavily on visual comparisons of porosity, saturation, concentration, streamlines, and temperature fields. The results section would be significantly stronger with quantitative metrics such as the following:

- breakthrough time and PVBT versus injection temperature and velocity,
- reacted mineral volume,
- acid utilization efficiency,
- wormhole length, width, branching density, or localization index

At present, the conclusions are plausible, but not quantified to a level expected for a strong modeling paper.

Response: We thank the reviewer for the helpful suggestion regarding quantitative analysis of the simulation results. We agree that quantitative metrics are important for evaluating acidizing performance. However, we would like to clarify that the revised manuscript already includes several quantitative measures, particularly the pore volume to breakthrough (PVBT), which is one of the most widely used quantitative indicators in matrix acidizing studies for characterizing stimulation efficiency and dissolution behavior.

In the manuscript, PVBT values are explicitly reported and compared for different injection temperatures and injection velocities. For example, the simulations with injected acid temperatures of 290 K, 320 K, and 360 K produce PVBT values of 10.92, 6.39, and 3.12, respectively (marked as red). These results provide quantitative support for the conclusions regarding the influence of thermal and hydrodynamic conditions on wormhole formation and acidizing efficiency.

In addition to PVBT, the manuscript also presents quantitative comparisons through normalized pressure-drop evolution, saturation relative-error analysis, and breakthrough criteria. Therefore, the conclusions are not based solely on visual inspection of porosity and saturation fields.

At the same time, we agree that additional quantitative descriptors such as reacted mineral volume, wormhole localization indices, or branching-density measures could provide further characterization of the dissolution structures. However, these quantities are not yet standard or uniquely defined for the present two-phase thermal DBF framework and would require additional methodological development beyond the scope of the current study. To improve clarity, we have further emphasized the existing quantitative metrics in the revised manuscript and added additional explanations where appropriate.

Minor comments

1. The parameter table is informative, but it would benefit from the addition of a column describing the physical meaning of each parameter, as well as references to literature sources or notes on calibration.

Response: We thank the reviewer for this valuable suggestion. We agree that additional information regarding the physical meaning and sources of the model parameters would improve the clarity and reproducibility of the manuscript. Following the reviewer's recommendation, the parameter table has been revised by adding an additional column describing the physical meaning of each parameter. We have also added references to the corresponding literature sources where the parameter values were adopted or estimated.

For parameters that are not directly taken from previous studies, additional notes have been included to clarify whether they are assumed values, benchmark parameters, or numerically selected values used for stability and demonstration purposes in the present simulations. These revisions improve the transparency of the numerical setup and make the parameter selection procedure clearer to readers

2. The section titled “Verification experiments” should be revised. It does not represent verification in the conventional computational science sense; a more appropriate title would be “Additional parametric study” or similar.

Response: We have modified it accordingly.

3. While the conclusions clearly summarize the results, they should more carefully distinguish between findings that are directly supported by the simulations and those that remain speculative or interpretive.

Response: We thank the reviewer for this helpful comment. We agree that the original conclusion section did not sufficiently distinguish between observations directly supported by the present simulations and broader interpretations or future perspectives. In response, we have revised the conclusion section to more clearly separate the numerical findings demonstrated in the current study from speculative discussions and potential future developments.

4. The quality of the figures should be improved to ensure high-resolution output. In addition, some figure titles appear to be inaccurate and should be corrected for clarity and consistency.

Response: Several figure titles and captions have been revised for improved clarity, accuracy, and consistency throughout the manuscript. In particular, ambiguous or repetitive descriptions have been corrected, and the terminology used in the captions has been unified to better match the corresponding simulation conditions and physical quantities presented in the figures. These revisions improve the overall readability and professionalism of the manuscript.

Two-Phase Thermal Simulation of Matrix Acidization Using the Non-Isothermal Darcy–Brinkman–Forchheimer Model

Yuanqing Wu[1], Jisheng Kou[2,3]

[1]School of Computer Science and Technology, Dongguan University of Technology, Dongguan 523808, Guangdong, China
[2]State Key Laboratory of Intelligent Deep Metal Mining and Equipment, Shaoxing University, Shaoxing 312000, Zhejiang, China
[3]Zhejiang Key Laboratory of Rock Mechanics and Geohazards，School of Civil Engineering, Shaoxing University, Shaoxing 312000, Zhejiang, China

Correspondence to: Jisheng Kou (jishengkou@163.com)

Abstract. This study presents a comprehensive two-phase thermal model for simulating matrix acidization in porous media using the non-isothermal Darcy–Brinkman–Forchheimer framework. The model integrates multiphase flow, reactive transport, dynamic porosity evolution, and heat transfer, with temperature-dependent reaction kinetics incorporated through an Arrhenius-type formulation. A series of numerical experiments are conducted to investigate the effects of initial matrix temperature, injected acid temperature, and injection velocity on dissolution behaviour and wormhole formation. Results show that the initial matrix temperature has minimal influence due to rapid thermal equilibrium, while high acid temperature significantly enhances reaction rates and promote localized wormhole growth. Verification experiments confirm that increasing acid temperature produces effects similar to decreasing injection velocity, as both shift the dissolution pattern from uniform to ramified and wormhole-dominated regimes. These findings offer valuable insights for optimizing acidizing treatments by balancing thermal and hydrodynamic conditions to improve stimulation efficiency.

1. Introduction

Matrix acidizing is a widely used stimulation technique in the petroleum industry aimed at enhancing the productivity of hydrocarbon reservoirs, particularly in carbonate and sandstone formations. The process involves injecting reactive acid solutions—commonly hydrochloric acid—into the reservoir at pressures below the fracture pressure, allowing the acid to flow through the porous matrix and dissolve mineral components that block pore spaces. This dissolution improves the permeability of the formation, facilitating more efficient oil and gas flow to the wellbore. Matrix acidizing is especially important in carbonate reservoirs, where it can lead to the formation of high-conductivity channels known as wormholes, significantly boosting well performance. As a cost-effective and controllable stimulation method, matrix acidizing plays a crucial role in maximizing recovery from existing wells

---

and extending the productive life of mature fields (Araújo et al., 2024; Mahdavi Kalatehno et al., 2025; Qureshi et al., 2023).

Numerical simulation is a crucial method for studying matrix acidizing. The evolution of numerical models for matrix acidizing can be summarized as follows: The earliest single-phase model, based on the Darcy scale, was introduced by (Daccord et al., 1993a, 1993b; Fredd and Fogler, 1998). (Golfier et al., 2002) later evaluated the Darcy-scale model's ability to capture different dissolution regimes and assess how flow parameters influence wormhole development. (Panga et al., 2005) advanced the field by proposing the two-scale model (Darcy scale and pore scale), which describes transport and reaction mechanisms in reactive dissolution and studies wormhole formation during carbonate core acidization. However, these models rely solely on Darcy's equation, which fails to accurately represent fluid dynamics in high-porosity regions that form during acidizing. As porosity increases—sometimes approaching unity in certain zones—Darcy's law becomes inadequate. Additionally, fluid velocities in these regions can rise significantly. To address this limitation, (Wu et al., 2015) introduced the Darcy-Brinkman-Forchheimer (DBF) model, incorporating Brinkman and Forchheimer terms into the momentum equations to better describe fluid dynamics in high-porosity conditions. Later, (Wu et al., 2022) combined the DBF framework with a continuum fracture model to simulate matrix acidization in fractured porous media, achieving accurate results with a simplified approach. The DBF framework has also been widely applied in other research areas, as seen in studies by (Alokaily, 2022; Deb et al., 2024; Shahid et al., 2025; Yoon and Mallikarjunaiah, 2025).

However, the models above assume a single water phase in the reservoir, with the acid dissolved within it. While single-phase models have been widely used in matrix acidizing studies due to their simplicity and computational efficiency, they exhibit severe limitations when applied to real reservoir conditions. A key drawback is the neglect of the oil phase, which is typically present in carbonate and sandstone formations during acidizing operations. This omission leads to an inability to capture essential two-phase flow dynamics, including capillary pressure, phase interference, and wettability-driven fluid redistribution—all of which critically influence acid accessibility and reaction efficiency (Rigi et al., 2025; Mahdavi Kalatehno et al., 2025). For example, in oil-wet systems, the presence of oil can hinder acid penetration into the matrix, modify dissolution patterns, and result in an underestimation of the pore volume required for breakthrough (Elsafih and Fahes, 2021). Additionally, single-phase models disregard saturation-dependent transport properties and chemical potential gradients, both of which play a vital role in accurately predicting wormhole development and treatment performance. While these simplified models are valuable for conceptual studies, their lack of two-phase physics limits their reliability for field-scale simulations and the optimization of acid stimulation treatments.

To address these challenges, researchers have developed two-phase two-scale continuum models by integrating traditional porous media flow theory with acidizing frameworks (Babaei and Sedighi, 2018; Wei et al., 2017). Notably, (Sabooniha et al., 2021) proposed a two-dimensional, two-phase model combining the Cahn–Hilliard phase-field theory with Navier–Stokes equations, solved numerically via the finite element method. Further advancing the field, (Ma et al., 2022) developed a three-dimensional two-phase acidizing model for fractured carbonate rocks, utilizing a unified pipe-network method alongside a sequential implicit time scheme and adaptive time-stepping to enhance simulation accuracy.

A critical challenge in carbonate acidizing is the formation of highly permeable flow channels, which significantly alter flow dynamics due to the combined effects of fluid viscosity and inertia. While most existing studies model these flows using Darcy's law alone, this approach neglects key factors such as viscous shear and inertial forces. A more robust alternative is the DBF model, which incorporates Darcy's law, the Brinkman term, and the Forchheimer correction, making it suitable for high-velocity flows and heterogeneous porous media. However, despite its advantages, the DBF model has been applied only to single-phase acidizing simulations (Kou et al., 2016, 2019; Wu and Ye, 2019), leaving its potential in two-phase systems unexplored. Thus, integrating the two-phase model with the DBF model is one contribution of this work.

The conventional DBF framework accounts only for mass and momentum conservation, neglecting the energy conservation equation. However, temperature variations—whether due to reservoir conditions or reaction heat—play a critical role in matrix acidizing. For instance, (Zhou et al., 2022) demonstrated that elevated temperatures significantly enhance the optimal acid injection rate, while (Jia et al., 2021) highlighted the pronounced influence of reaction temperature at higher injection rates. Their findings further indicate that the optimal injection rate decreases with increasing activation energy or decreasing acid diffusion coefficient, underscoring the necessity of incorporating thermal effects into acidizing models. To address this gap, (Wu et al., 2021) extended the single-phase DBF model by integrating the energy conservation equation, forming a thermal DBF framework capable of capturing temperature-dependent dynamics. However, this model remains limited by its single-phase assumption, restricting its applicability to real-world reservoir conditions, which typically involve multiphase flow. Therefore, this work advances the field by developing a novel two-phase thermal DBF model, representing a key contribution to the understanding of heat-fluid interactions in acidizing processes.

The proposed two-phase thermal DBF model addresses the limitations of traditional single-phase and isothermal frameworks by integrating several key physical mechanisms into a unified formulation. First, it incorporates multiphase momentum conservation by coupling the DBF equations with relative permeability functions, allowing for accurate representation of viscous and inertial effects in both water and oil phases. Second, it introduces energy conservation with interphase mass exchange, capturing heat transfer processes alongside acid–rock reactions and dissolution-induced phase changes. Third, the model features temperature-dependent reaction kinetics governed by Arrhenius-type relationships, enabling spatially resolved predictions of reaction rates under varying thermal conditions. Together, these components empower the model to simulate complex field phenomena, including thermally driven wormhole branching, rate optimization guided by thermal feedback, and quantification of competing effects between reaction enthalpy and viscous dissipation in multiphase systems. This work thus establishes the first comprehensive two-phase thermal DBF framework, effectively representing a methodological step toward more realistic modeling of multiphase thermal acidizing processes. This work is organized as following.

Deleted: with high fidelity

Deleted: bridging the gap between idealized models and practical field applications where multiphase flow and thermal effects are inherently coupled. represent

Introduction: Presents the need for a thermal two-phase acidizing model to address limitations in existing single-phase or isothermal approaches.

Numerical Model: Formulates the coupled mass, momentum, energy, and species transport equations with temperature-dependent reaction kinetics.

Solution Procedure: Describes the discretization and solution procedure to implement the model. Numerical Experiments: Shows some important conclusions from the numerical experiments. Conclusion and Future Work: Summarizes key findings on how thermal and flow conditions govern acidizing efficiency. Outlines extensions to heterogeneous media, larger scales, multi-mineral systems, and optimization tools.

2. Numerical Model

The two-phase thermal DBF model includes the mass conservation equation for each fluid phase $\alpha \in \{w, n\}$, which is expressed as below. w represents the wetting phase such as the water phase, and n stands for the non-wetting phase such as the oil phase.

$$\frac{\partial(\phi S_\alpha)}{\partial t} + \nabla \cdot (\phi S_\alpha \boldsymbol{u_\alpha}) = 0, \tag{1}$$

In the equation, ϕ is the porosity, S_α is the saturation of phase α, $\boldsymbol{u_\alpha}$ is the effective velocity of phase α, and t is the time. This equation does not consider any source or sink term, and the fluid is incompressible. Based on the single-phase DBF equation, the DBF equation for the two-phase condition (the momentum conservation equation) is expressed as:

$$\rho_\alpha \left(\frac{\partial(\phi S_\alpha \boldsymbol{u_\alpha})}{\partial t} + \nabla \cdot (\phi S_\alpha \boldsymbol{u_\alpha} \otimes \boldsymbol{u_\alpha}) \right)$$

$$= -\nabla(p + \mu_\alpha) - \frac{\eta_\alpha \phi S_\alpha}{k_{r\alpha} \boldsymbol{K}} \boldsymbol{u_\alpha} + \nabla \cdot \phi S_\alpha \eta_\alpha \nabla \boldsymbol{u_\alpha} - \phi S_\alpha \rho_\alpha F_\alpha |\boldsymbol{u_\alpha}| \boldsymbol{u_\alpha} + \rho_\alpha \boldsymbol{g}, \tag{2}$$

where p is the fluid pressure, μ_α is the capillary pressure potential of phase α, η_α is the dynamic viscosity, $\boldsymbol{K}$ is the absolute permeability, $k_{r\alpha}$ is the relative permeability, ρ_α is the mass density of phase α, F_α is the Forchheimer drag coefficient, and $\boldsymbol{g}$ is the gravity. The fluid is assumed as the Newtonian fluids (constant viscosity). The chemical potential μ_α due to capillary effects is defined as (Kou et al., 2021,2023,2024):

$$\mu_w = \gamma_w \ln(S_w) + \gamma_{wn} S_n, \tag{3}$$

$$\mu_n = \gamma_n \ln(S_n) + \gamma_{wn} S_w, \tag{4}$$

with the saturation constraint

$$S_w + S_n = 1, \tag{5}$$

where γ_w, γ_n, and γ_{wn} are phenomenological constants related to fluid-fluid interactions. The transport of reactant (acid) concentration C_f in the wetting phase is governed by:

$$\frac{\partial(\phi S_w C_f)}{\partial t} + \nabla \cdot \left(\phi S_w \boldsymbol{u_w} C_f\right) - \nabla \cdot \left(\phi S_w \boldsymbol{D}_e \cdot \nabla C_f\right) = -\frac{S_w a_v k_s k_c C_f}{k_c + k_s}, \tag{6}$$

where $\boldsymbol{D}_e$ is the effective diffusivity, a_v is the specific surface area per unit volume, k_c, k_s are reaction rate constants for mass transfer and surface reaction, respectively. The porosity-progress equation is modeled as:

$$\frac{\partial \phi}{\partial t} = \frac{\alpha S_w a_v k_s k_c C_f}{\rho_s (k_c + k_s)}, \tag{7}$$

where ρ_s is the solid matrix density, α is a stoichiometric coefficient.

All the equations above are established with the constant-temperature assumption. However, it is known that temperature is an important factor to influence the chemical reaction in reservoirs. Thus, to consider the temperature effect, we introduce the energy conservation equation as following.

$$\sum_{\alpha=w,n} \rho_\alpha \theta_\alpha \frac{\partial(\phi S_\alpha T)}{\partial t} + \rho_s \theta_s \frac{\partial((1-\phi)T)}{\partial t} + \sum_{\alpha=w,n} \rho_\alpha \theta_\alpha \nabla \cdot (\phi S_\alpha \boldsymbol{v}_{\boldsymbol{\alpha}} T)$$

$$-\nabla \cdot (\phi S_w M_w + \phi S_n M_n + (1-\phi) M_s) \nabla T$$

$$= -2 H_r a_v k_e C_f + \sum_{\alpha=w,n} (\frac{\eta_\alpha \phi S_\alpha}{k_{r\alpha} \boldsymbol{K}} |\boldsymbol{v}_{\boldsymbol{a}}|^2 + \eta_\alpha \phi S_\alpha |\nabla \boldsymbol{v}_{\boldsymbol{a}}|^2 + \phi S_\alpha \rho_\alpha F_\alpha |\boldsymbol{v}_{\boldsymbol{a}}|^3), \tag{8}$$

where T stands for the temperature, θ_α is the specific heat capacity of the phase α, M_α is the thermal conductivity of the phase α. H_r is the reaction heat, which is expressed as

$$H_r = -6846 + 8.038T - 0.00322T^2 - 870.3T^{-1}. \tag{9}$$

Besides that, k_e is a coefficient, which is defined as

$$k_e = \frac{2k_c k_s}{k_c + 2k_s}. \tag{10}$$

The value of the molecular diffusion coefficient d_m depends on the temperature directly, which is called the Arrhenius-type dependencies. It can be expressed as

$$d_m = d_{m0} \cdot e^{\frac{E_g}{R_g}(\frac{1}{T_0} - \frac{1}{T})}. \tag{11}$$

The subscript “0” stands for the initial value. E_g is the activation energy, and R_g is the molar gas constant. Moreover, k_s also has the Arrhenius-type dependencies, which is expressed as

$$k_s = k_{s0} \cdot e^{\frac{E_g}{R_g}(\frac{1}{T_0} - \frac{1}{T})}. \tag{12}$$

By the temperature-dependent parameters above, the reaction term in the concentration equation (6) and the porosity equation (7) are affected by the temperature.

The equations form a fully coupled, nonlinear system that integrates two-phase flow dynamics, momentum transport, reactive acid dissolution, porosity evolution, and temperature changes to accurately simulate wormhole formation during acidizing operations. Temperature effects are critically incorporated through Arrhenius-type dependencies for molecular diffusion (d_m) and surface reaction rates (k_s), which directly influence acid transport (via the acid concentration equation) and porosity development (via the porosity-progress equation). The evolving porosity then feeds back into the mass and momentum conservation equations by modifying permeability and pore structure parameters, while the computed flow velocities and reaction rates determine heat generation in the energy conservation equation. This bidirectional coupling creates a continuous feedback loop: updated temperature values alter reaction kinetics and transport properties, which in turn affect fluid flow and dissolution patterns. The model's ability to capture these complex thermo-hydro-chemical interactions enables precise prediction of wormhole propagation under realistic reservoir conditions, providing valuable insights for optimizing stimulation treatments through comprehensive parameter sensitivity analysis and performance evaluation.

In the system, S_w, ϕ, p, $\boldsymbol{u_\alpha}$, C_f and T are the main unknowns to be solved by the numerical schemes mentioned later. The other variables can be computed by the following equations. The Forchheimer drag coefficient is calculated as

$$F_\alpha = \frac{1.75}{\sqrt{150(S_\alpha \phi)^3}}. \tag{13}$$

The relative permeability is

$$k_{r\alpha} = {S_\alpha}^3. \tag{14}$$

$\boldsymbol{D_e}$ is expressed as

$$\boldsymbol{D_e} = \alpha_{OS} d_m \boldsymbol{I} + \frac{\|\boldsymbol{u_w}\|}{\phi S_w}(d_l \boldsymbol{E} + d_t \boldsymbol{E}^\perp). \tag{15}$$

In 2D condition,

$$\boldsymbol{E} = \frac{1}{\|\boldsymbol{u_w}\|^2}\begin{pmatrix} u_{wx}^2 & u_{wx}u_{wy} \\ u_{wy}u_{wx} & u_{wy}^2 \end{pmatrix}, \tag{16}$$

$$\boldsymbol{E}^\perp = \boldsymbol{I} - \boldsymbol{E}. \tag{17}$$

u_{wx}、u_{wy} stand for the wetting-phase velocity of the *x*- and *y*-directions, respectively. d_l and d_t stand for the longitudinal dispersion coefficient and the transverse dispersion coefficient, respectively.

$$d_l = \alpha_{OS} d_m + \frac{2\lambda_X \|\boldsymbol{u}\| r_p}{\phi}, \tag{18}$$

$$d_t = \alpha_{OS} d_m + \frac{2\lambda_T \|\boldsymbol{u}\| r_p}{\phi}. \tag{19}$$

α_{OS} is a constant depending on pore connectivity. λ_X and λ_T are constants depending on the structure of the medium. Besides that, there are Kozeny-Carman equations as below

$$\frac{K}{K_0} = \frac{\phi}{\phi_0}\left(\frac{\phi(1-\phi_0)}{\phi_0(1-\phi)}\right)^2, \tag{20}$$

$$\frac{r_p}{r_0} = \sqrt{\frac{K\phi_0}{K_0\phi}}, \tag{21}$$

$$\frac{a_v}{a_0} = \frac{\phi r_0}{\phi_0 r_p}. \tag{22}$$

If the matrix is homogeneous, the permeability value K can be represented as a scalar. Based on Eq. (20), K can be directly calculated once ϕ is known. Furthermore, by combining Eqs. (20) - (22), the parameter a_v can be expressed as a function of ϕ, enabling its determination. r_p is the pore radius. k_c is calculated from Eq. (23).

$$k_c = \frac{d_m}{2r_p}\left(Sh_\infty + 0.7\left(\frac{2\|\boldsymbol{u_w}\| r_p \rho_w}{\eta_w}\right)^{\frac{1}{2}}\left(\frac{\eta_w d_m}{\rho_w}\right)^{\frac{1}{3}}\right), \tag{23}$$

where Sh_∞ is the asymptotic Sherwood number.

3. Solution Procedure

The strongly coupled nonlinear equation system presents significant computational challenges due to its inherent complexity. To address this, we employ a structured numerical approach using a uniform grid with spatial resolutions Δx and Δy in the respective coordinate directions, along with uniform time steps Δt for temporal discretization. The solution adopts a staggered grid arrangement, with primary variables (water saturation S_w, porosity ϕ, pressure p, acid concentration C_f, and temperature T) stored at cell centers while phase velocities $\boldsymbol{u_\alpha}$ are defined at cell edges. Spatial approximations are carefully implemented: harmonic averaging is applied for edge porosity and permeability using adjacent cell-center values, while arithmetic averaging is used for nodal porosity and saturation calculations. The scheme employs upwind discretization for both edge saturations and acid concentrations to ensure numerical stability. The gradients can be derived with the finite difference method. This conservative formulation maintains proper mass balance while effectively handling the complex coupling between multiphase flow, reactive transport, evolving porosity-permeability relationships, and temperature change that characterize the acidizing process.

To solve the coupled system, it is first necessary to define a consistent solution sequence for the primary unknowns. The porosity ϕ^{n+1} is updated first, as it is directly governed by the porosity evolution equation (Eq. (7)), which is relatively straightforward. A first-order backward Euler scheme is used for time discretization throughout the model. Applying this scheme to Eq. (7) allows for the explicit computation of the updated porosity at the beginning of each time step, where the superscript n denotes the previous time level. Once porosity is updated, the next step is to solve for the wetting-phase saturation S_w^{n+1}. This requires discretizing the wetting-phase mass conservation equation (Eq. (1)), which leads to a linear system in which S_w^{n+1} is the unknown. Solving this system yields the new saturation field. Following this, the model proceeds to solve for pressure p^{n+1} and phase velocities $\boldsymbol{u_\alpha^{n+1}}$ simultaneously, using a coupled formulation of the momentum and mass conservation equations. To do so, the mass conservation equations for both wetting and non-wetting phases are summed to yield a unified continuity equation:

$$\frac{\partial \phi}{\partial t} + \sum_{\alpha=w,n}(\nabla \cdot (\phi S_\alpha \boldsymbol{u_\alpha})) = 0. \tag{24}$$

This equation, in combination with the momentum equation (Eq. (2)), is discretized to form a linear system in which the unknowns are p^{n+1} and $\boldsymbol{u_\alpha^{n+1}}$. Since the DBF momentum equation is nonlinear in velocity, appropriate linearization is performed: the advective term is approximated as $\nabla \cdot (\phi S_\alpha \boldsymbol{u_\alpha^n} \otimes \boldsymbol{u_\alpha^{n+1}})$, while the Forchheimer term is linearized as $\phi S_\alpha \rho_\alpha F_\alpha |\boldsymbol{u_\alpha^n}| \boldsymbol{u_\alpha^{n+1}}$. Once the velocity and pressure fields are updated, the acid concentration C_f^{n+1} is solved by discretizing the reactive transport equation (Eq. (6)), again yielding a linear system. The reaction source term is treated implicitly using values from the new time step. The final step in the solution sequence is the update of temperature T^{n+1}, governed by the energy conservation equation (Eq. (8)). Here, all temperature-dependent terms on the left-hand side are discretized implicitly (using T^{n+1}), while the source and transport terms on the right-hand side are discretized explicitly (using T^n). This approach yields a linear system for T^{n+1}, which can be solved to update the thermal field. This time-stepping procedure is repeated Iteratively until either the final simulation time is reached or breakthrough occurs. Breakthrough is defined as the moment when the pressure drop between the inlet and outlet boundaries decreases to within 1% of its initial value, indicating the formation of a high-conductivity channel. It is important to ensure that all auxiliary variables are updated prior to their use in the computation of the primary unknowns. The simulations are advanced using sufficiently small time-steps to ensure stable evolution of the coupled thermo-hydraulic-reactive system. The flowchart of the solution procedure is shown in **Figure 1**.

High-resolution simulation of matrix acidizing in porous media requires fine computational grids to accurately resolve porosity heterogeneity and capture wormhole dynamics. However, the resulting large-scale systems significantly increase computational demand. To address this, an efficient parallel computing strategy is developed, focusing on domain decomposition, inter-processor communication, and distributed solution of the coupled linear system. More details on the parallelization can be found in (Wu et al., 2015).

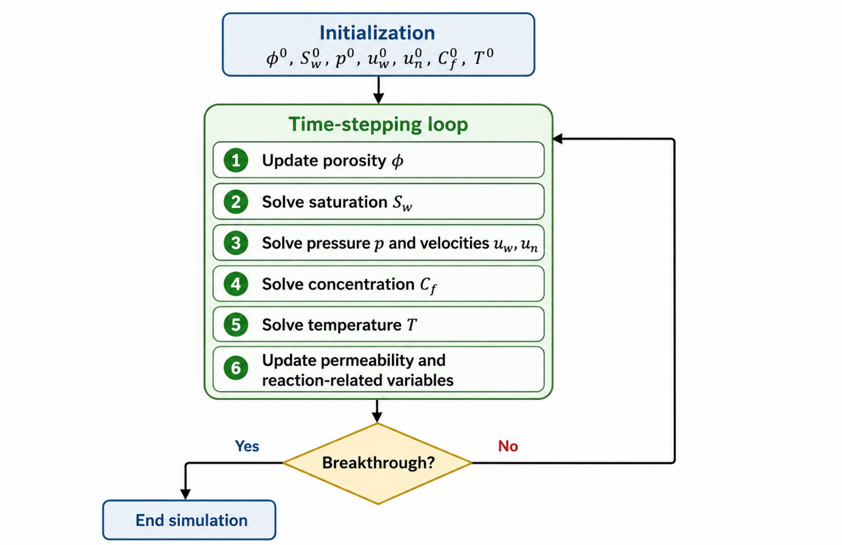

Figure 1 The flowchart of the solution procedure.

4. Numerical Experiments

4.1 Verification experiments

To verify the numerical implementation, a 2D two-phase nonreactive displacement benchmark is conducted. The computational domain is a rectangle of size 0.1 m × 0.1 m. In this benchmark, clear water rather than reactive acid is injected uniformly from the left boundary and exits through the right boundary, while the top and bottom boundaries are treated as impermeable. Since no chemical reaction is considered, the porosity remains constant at 0.2 throughout the simulation. Thermal effects are also neglected. Initially, the porous medium is partially saturated with water, with an initial water saturation of 0.2. Therefore, the problem reduces to immiscible water–oil displacement in a homogeneous two-dimensional porous medium.

Deleted: To verify the code

To further simplify the benchmark, the viscosities of the water and oil phases are both set to 1 Pa·s, and the densities of both phases are fixed at 1 kg/m³. Capillary pressure effects are neglected by setting γ_w, γ_n, and γ_{wn} to zero. Gravity is also ignored. The absolute permeability of the domain is prescribed as 1 m². Water is injected at a constant velocity of 1.0×10^{-4} m/s from the left boundary, while a zero-pressure condition is imposed at the right boundary. The remaining parameters are listed in **Table 1**.

Formatted: Superscript

To examine grid convergence, four different uniform meshes consisting of 40×40, 80×80, 120×120, and 160×160 cells are used to discretize the computational domain. The time step is fixed at 0.01 s for all simulations. The normalized pressure drop obtained from 6000 time-steps using the four different computational grids is presented in **Figure 2**. The pressure drop is defined as the absolute difference between the average pressures at the inlet and outlet boundaries of the domain. To facilitate comparison among different grid resolutions, the pressure drop is normalized by its initial value, resulting in the normalized pressure drop reported in the figure.

The figure demonstrates grid convergence of the numerical code. As the mesh is refined from 40×40 to 160×160, the normalized pressure-drop curves become progressively closer. The difference between the 120×120 and 160×160 results is much smaller than the difference between the coarser-grid results, indicating that the solution approaches a grid-independent limit. In particular, all four simulations show the same physical trend: the normalized pressure drop decreases monotonically with time as water displaces oil and the flow resistance is reduced. The finer-grid solutions preserve this trend while producing increasingly similar pressure-drop histories. Therefore, the pressure-drop response is not dominated by numerical discretization error, and the results suggest that the implemented two-phase flow solver is grid-convergent.

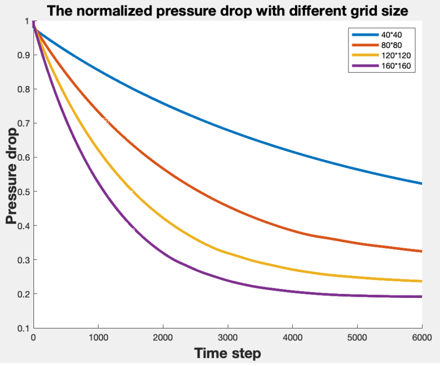

Figure 2 Normalized pressure drop evolution for the four computational grids.

Because the medium is homogeneous and the boundary conditions are uniform in the *y*-direction, the 2D solution should remain essentially one-dimensional: $S_w(x,y,t) \approx S_w(x,t)$. Thus, another simple numerical verification metric is:

Formatted: Font: Italic

$$E_y(t) = \frac{|S_w(x,y,t) - \overline{S_w}(x,t)|}{\overline{S_w}(x,t)}, \qquad (25)$$

Formatted: English (US)

Formatted: Els-equation

where

$$\overline{S_w}(x,t) = \frac{1}{L_y}\int_0^{L_y} S_w(x,y,t)\,dy. \qquad (26)$$

L_y stands for the length of the domain in the *y*-direction. Three representative points located on the left boundary of the computational domain are selected for monitoring. These points are positioned at heights of $\frac{L_y}{4}$ (down point), $\frac{L_y}{2}$ (middle point), and $\frac{3L_y}{4}$ (up point) measured from the bottom boundary. The temporal evolution of $E_y(t)$ at these three locations is presented in **Figure 3**.

For the coarse mesh of 40×40 cells, the relative errors increase continuously during the simulation and reach values on the order of 10^{-2}. In addition, noticeable differences are observed among the three monitoring points, indicating that the coarse grid is unable to accurately capture the evolution of the saturation front and therefore introduces relatively large discretization errors. After refining the mesh to 80×80 cells, the relative errors are significantly reduced. Although the errors still vary with time due to the propagation of the displacement front, the maximum error becomes considerably smaller than that of the 40×40 grid. This demonstrates that mesh refinement improves the numerical accuracy and enhances the spatial resolution of the two-phase displacement process. For the finest mesh of 160×160 cells, the relative errors decrease further and remain on the order of 10^{-3}, which is much smaller than those observed for the 40×40 grid. Furthermore, the error curves corresponding to the three monitoring points exhibit very similar trends and remain small throughout the entire simulation. This indicates that the numerical solution becomes increasingly insensitive to additional mesh refinement. Overall, the results in **Figure 3** clearly show that $E_y(t)$ is very small and decreases with mesh refinement, which demonstrates the correctness of the 2D implementation.

Formatted: English (US)

Formatted: Els-equation

Formatted: Font: Italic

Formatted: Superscript

Formatted: Superscript

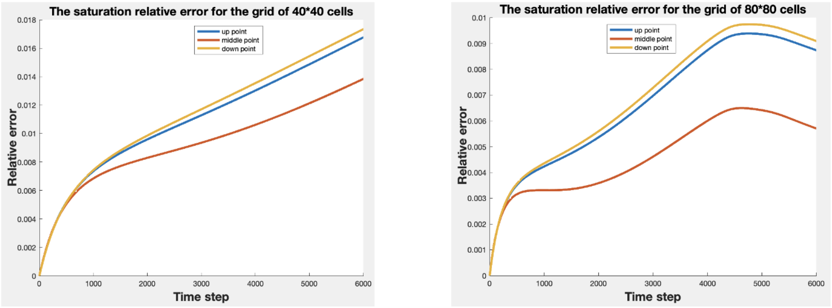

(a) The saturation relative error for the grid of 40*40 cells.

(b) The saturation relative error for the grid of 80*80 cells.

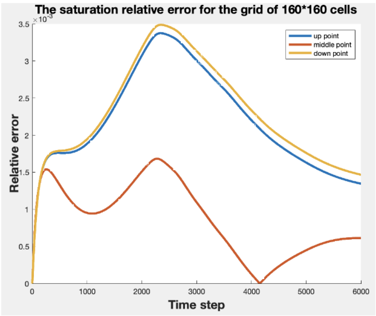

(c) The saturation relative error for the grid of 160*160 cells.

Figure 3 The saturation relative error for different computing grids.

4.2 Experiments with different initial matrix temperatures

To investigate the influence of the initial matrix temperature on two-phase acidizing, three numerical experiments on single-reactive-mineral carbonate matrix are conducted, each with a constant acid injection temperature but different initial matrix temperatures. The injection temperature of the acid is maintained at 320 K, while the initial matrix temperatures are set to 320 K, 420 K, and 520 K, respectively. The computational domain is a rectangular matrix measuring 0.1 m × 0.1 m, discretized into a uniform grid of 120 × 120 cells. Initially, the matrix is nearly saturated with oil, with a water saturation of 0.01. Acid is injected from the left boundary at a constant velocity of 4.17×10^{-5} m/s, resulting in a water saturation of 1.0 at that boundary. The injected acid has a concentration of 500 mol/m^3. The right boundary serves as the outflow, while the top and bottom boundaries are impermeable. To represent natural heterogeneity, the initial porosity is spatially randomized with an average value of 0.18. To that end, the function "random_number (rand)" in FORTRAN90 is used to generate an array of pseudorandom numbers from the uniform distribution over the range [0, 1]. Then, the numbers in [0, 1] is mapped to another range [0.15, 0.21] by the formulation: new_rand = 0.06*rand + 0.15. The average value of new_rand in [0.15, 0.21] is 0.18. Gravity is applied in the *y*-direction. The relevant physical and chemical parameters used in the simulations are summarized in Table 1. The simulation is performed with a time step of ten seconds, and the UMFPACK solver is employed for solving the resulting linear systems.

Deleted: ¶

Deleted: Table 1

Table 1 Physical and chemical parameters of the experiments

Parameter	**Value**	**Unit**	**Physical meaning**	**Source/note**
$\boldsymbol{a_{v0}}$	5.0×10^{-1}	m^{-1}	Initial specific surface area	Adopted from literature
$\boldsymbol{C_{f,\mathrm{in}}}$	5.0×10^{2}	$\mathrm{mol/m}^{3}$	Injected acid concentration	Simulation co
$\boldsymbol{d_{m0}}$	3.6×10^{-9}	$\mathrm{m}^{2}/\mathrm{s}$	Initial molecular diffusion coefficient	Adopted from studies
$\boldsymbol{g_{y}}$	-9.807	$\mathrm{m/s}^{2}$	Gravitational acceleration in *y*-direction	Physical const
$\boldsymbol{K_{0}}$	9.869233×10^{-16}	m^{2}	Initial permeability	Representative carbonate permeability
$\boldsymbol{k_{s0}}$	2.0×10^{-3}	$\mathrm{m/s}$	Initial surface reaction rate constant	Adopted from literature
$\boldsymbol{M_{n}}$	1.5×10^{1}	$\mathrm{W/(m \cdot K)}$	Thermal conductivity of oil phase	Assumed thermophysical property
$\boldsymbol{M_{s}}$	5.526×10^{2}	$\mathrm{W/(m \cdot K)}$	Thermal conductivity of solid matrix	Assumed thermophysical property
$\boldsymbol{M_{w}}$	6.0×10^{1}	$\mathrm{W/(m \cdot K)}$	Thermal conductivity of water phase	Assumed thermophysical property
$\boldsymbol{r_{0}}$	1.0×10^{-6}	m	Initial pore radius	Representative scale parameter
$\boldsymbol{Sh_{\infty}}$	3.66		Asymptotic Sherwood number	Classical mass correlation
$\boldsymbol{\alpha}$	5.0×10^{-2}	$\mathrm{kg/mol}$	Stoichiometric coefficient	Adopted from model
$\boldsymbol{\alpha_{OS}}$	5.0×10^{-1}		Medium structure coefficient	Assumed poro medium parameter
$\boldsymbol{\gamma_{n}}$	0.0	$\mathrm{Pa \cdot s}$	Oil-phase capillary coefficient	Adopted from studies
$\boldsymbol{\gamma_{w}}$	5.8×10^{2}	$\mathrm{Pa \cdot s}$	Water-phase capillary coefficient	Adopted from studies
$\boldsymbol{\gamma_{wn}}$	0.0	$\mathrm{Pa \cdot s}$	Interfacial capillary coefficient	Adopted from studies

Formatted Table
Formatted: Left
Formatted: Left
Formatted: Left
Formatted: Left
Formatted: Font: Italic
Formatted: Left
Formatted: Left
Formatted: Left
Formatted: Left
Formatted: Left
Formatted: Left
Formatted: Left
Formatted: Left
Formatted: Left
Formatted: Left
Formatted: Left
Formatted: Left

$\boldsymbol{\eta_n}$	1.0×10^{-2}	$\mathrm{Pa \cdot s}$	Dynamic viscosity of oil phase	Typical reserv value
$\boldsymbol{\eta_w}$	1.0×10^{-3}	$\mathrm{Pa \cdot s}$	Dynamic viscosity of water phase	Standard fluid
$\boldsymbol{\theta_n}$	2.0×10^{2}	$\mathrm{J/(kg \cdot K)}$	Specific heat capacity of oil phase	Assumed thermophysical property
$\boldsymbol{\theta_s}$	2.0×10^{1}	$\mathrm{J/(kg \cdot K)}$	Specific heat capacity of solid matrix	Assumed thermophysical property
$\boldsymbol{\theta_w}$	4.184×10^{2}	$\mathrm{J/(kg \cdot K)}$	Specific heat capacity of water phase	Standard thermodynamic value
$\boldsymbol{\lambda_T}$	1.0×10^{-1}		Transverse dispersivity coefficient	Typical porous parameter
$\boldsymbol{\lambda_X}$	5.0×10^{-1}		Longitudinal dispersivity coefficient	Typical porous parameter
$\boldsymbol{\rho_n}$	9.0×10^{2}	$\mathrm{kg/m^3}$	Density of oil phase	Typical reserv value
$\boldsymbol{\rho_s}$	2.71×10^{3}	$\mathrm{kg/m^3}$	Density of solid matrix	Typical carbon value
$\boldsymbol{\rho_w}$	1.01×10^{3}	$\mathrm{kg/m^3}$	Density of water phase	Standard fluid
$\boldsymbol{\Phi_0}$	1.8×10^{-1}		Average initial porosity	Simulation co

Formatted: Left

Formatted: Left

Formatted: Left

Formatted: Left

Formatted: Left

Formatted: Left

Formatted: Left

Formatted: Left

Formatted: Left

Formatted: Left

Formatted: Font: Not Italic

Formatted: Left

Formatted: Font: Not Italic

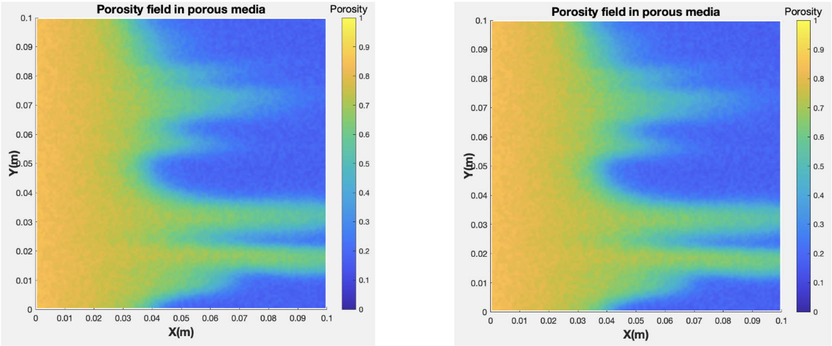

(a) Porosity profile with initial matrix temperature of 320 K.

(b) Porosity profile with initial matrix temperature of 420 K.

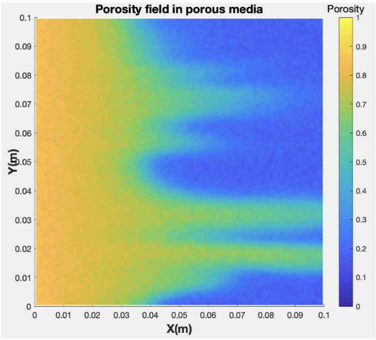

(c) Porosity profile with initial matrix temperature of 520 K.

Figure 4 Porosity profiles of the two-phase experiments at breakthrough with different initial matrix temperatures.

Deleted: 1

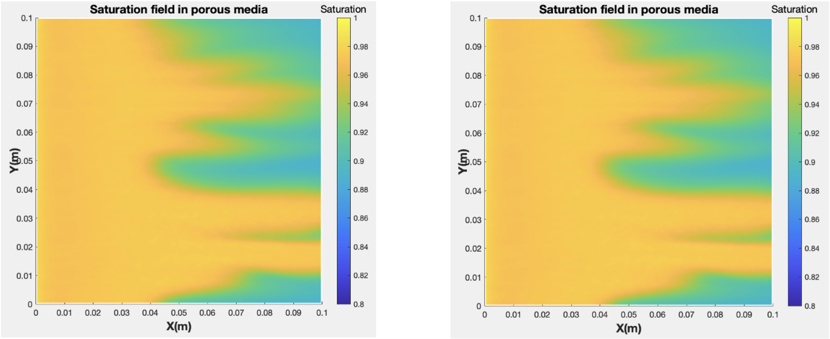

(a) Saturation profile with initial matrix temperature of 320 K.

(b) Saturation profile with initial matrix temperature of 420 K.

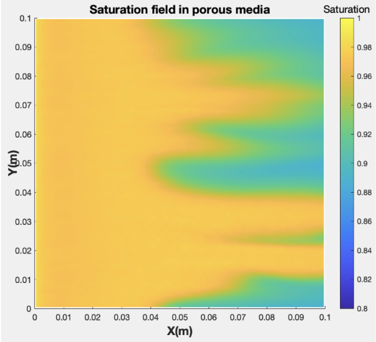

(c) Saturation profile with initial matrix temperature of 520 K.

Figure 5 Saturation profiles of the two-phase experiments at breakthrough with different initial matrix temperatures.

The numerical simulations reveal that variations in the initial matrix temperature—set at 320 K, 420 K, and 520 K—do not lead to significant differences in the outcome of the two-phase acidizing process. Across all three cases, the acid is injected at a constant temperature of 320 K, and the simulation is run until breakthrough, which occurs when the pressure differential between inlet and outlet stabilizes within 1% of its initial value. The computed pore volume to breakthrough (PVBT) is 6.392 in all scenarios, suggesting that the overall rate of acid propagation and dissolution behavior is largely insensitive to the initial thermal state of the matrix.

This conclusion can also be drawn from Figure 4 and Figure 5. The two figures show that the porosity and saturation profiles at breakthrough are highly similar across the three temperature settings. The acid-induced dissolution patterns develop with nearly identical wormhole morphologies, and the acid front progresses in a comparable manner through the porous medium. This indicates that, under the given conditions, the chemical reaction kinetics and transport processes are predominantly governed by the injected acid properties and flow dynamics, rather than the initial temperature of the solid matrix.

However, the little differences of the simulation results among different initial matrix temperature in Figure 4 and Figure 5 cannot be clarified by eyeballs. Thus, the differences in average porosity between different initial matrix temperatures during the simulation are given in Figure 6. From the

Deleted: 2

Formatted: Font color: Red

Deleted: Figure 1

Deleted: Figure 2

Deleted: figures show t

Deleted: Figure 1

Deleted: Figure 2

Deleted: Figure 3

figure, it is clearly seen that the differences between different initial matrix temperatures are in the order of 10^{-7} and 10^{-8}, respectively, which demonstrates the negligible influence of initial matrix temperatures on acidizing.

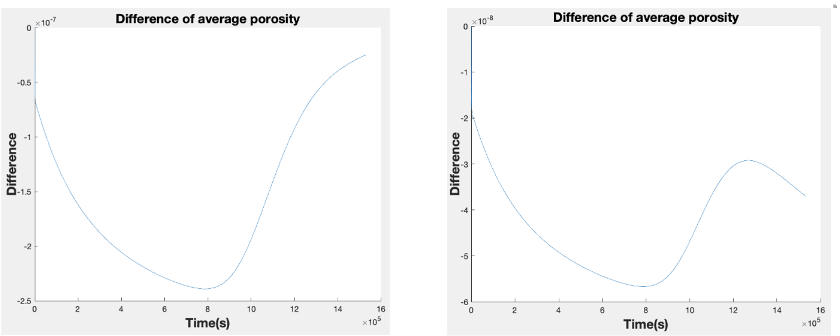

(a) The difference in average porosity between matrices with initial temperatures of 320 K and 420 K.

(b) The difference in average porosity between matrices with initial temperatures of 420 K and 520 K.

Figure 6 Differences in average porosity between different initial matrix temperatures during the simulation

Deleted: 3

4.3 Experiments with different acid temperatures

Since the acidizing process shows minimal sensitivity to the initial matrix temperature, this section focuses on investigating the influence of the injected acid temperature on the acidizing behavior. The initial matrix temperature is fixed at 420 K, while the injection temperatures are varied, set at 290 K and 360 K, respectively. It is noted that the range of the acid temperature is generally between 273 K and 373 K in real applications, and therefore the acid temperatures outside the range are not considered. The simulation is performed with a time step of one second. All other experimental conditions remain largely consistent with those described in the previous section.

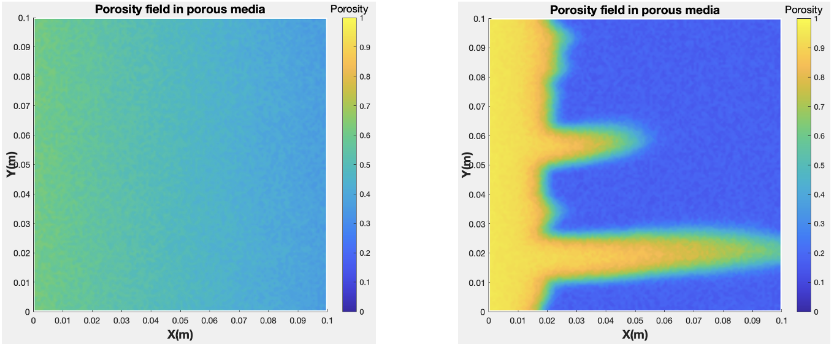

(a) Porosity profile with initial matrix temperature of 290 K.

(b) Porosity profile with initial matrix temperature of 360 K.

Figure 7 Porosity profiles of the two-phase experiments at breakthrough with different acid temperatures.

Deleted: 4

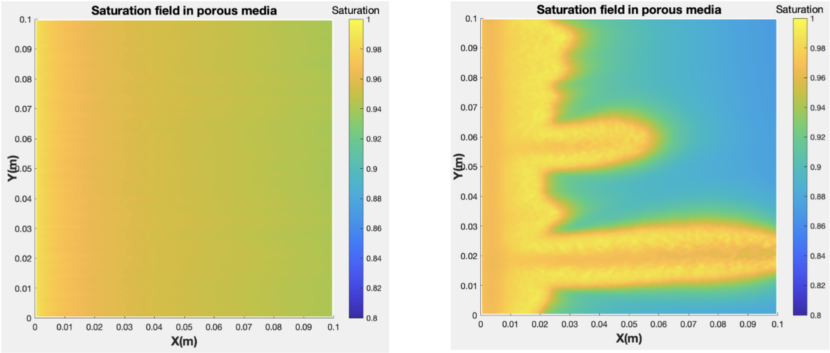

(a) Saturation profile with initial matrix temperature of 290 K.

(b) Saturation profile with initial matrix temperature of 360 K.

Figure 8. Saturation profiles of the two-phase experiments at breakthrough with different acid temperatures.

Deleted: 5

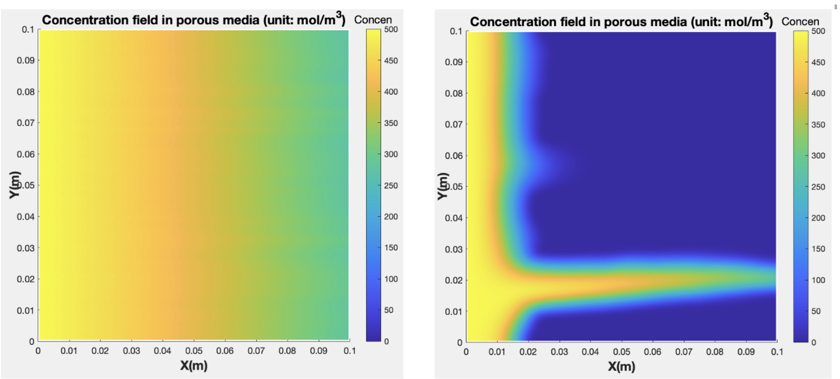

(a) Concentration profile with initial matrix temperature of 290 K.

(b) Concentration profile with initial matrix temperature of 360 K.

Figure 9. Concentration profiles of the two-phase experiments at breakthrough with different acid temperatures.

Deleted: 6

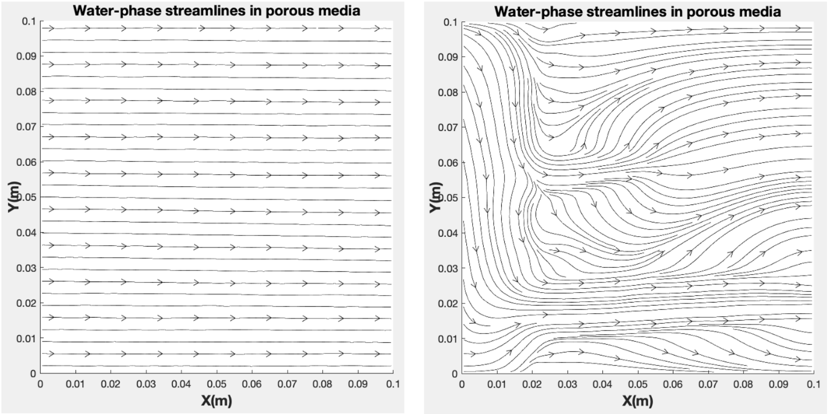

(a) Water-phase streamlines with initial matrix temperature of 290 K. (b) Water-phase streamlines with initial matrix temperature of 360 K.

Figure 10. Water-phase streamlines of the two-phase experiments at breakthrough with different acid temperatures.

Deleted: 7

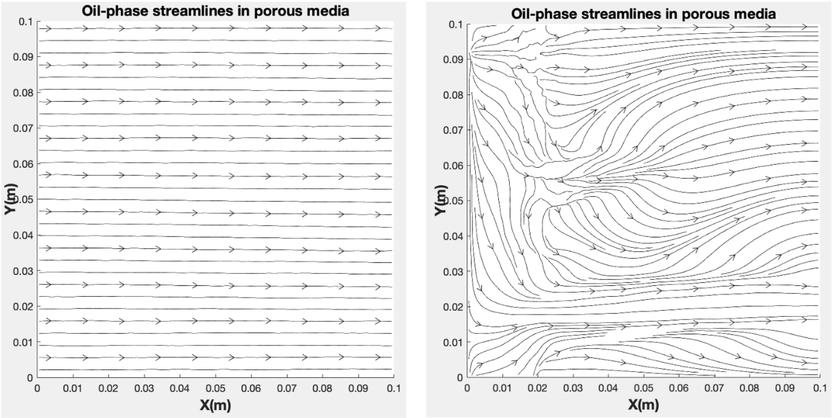

(a) Oil-phase streamlines with initial matrix temperature of 290 K. (b) Oil-phase streamlines with initial matrix temperature of 360 K.

Figure 11. Oil-phase streamlines of the two-phase experiments at breakthrough with different acid temperatures.

Deleted: 8

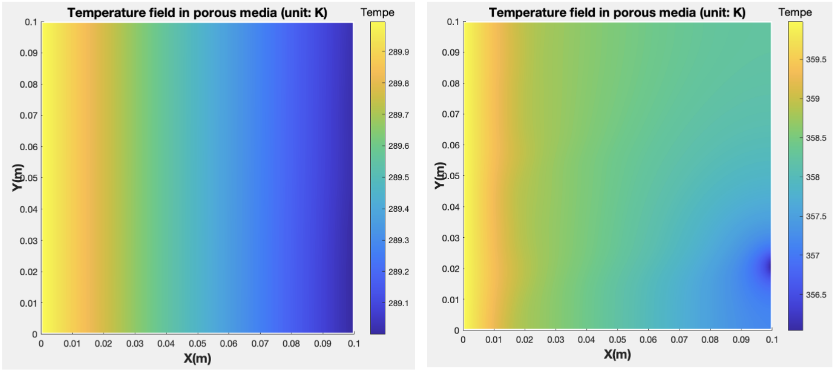

(a) Temperature profile with initial matrix temperature of 290 K. (b) Temperature profile with initial matrix temperature of 360 K.

Figure 12 Temperature profiles of the two-phase experiments at breakthrough with different acid temperatures.

Deleted: 9

This section explores the effect of injected acid temperature on the two-phase acidizing process while keeping the initial matrix temperature constant at 420 K. Three scenarios are examined: acid injection temperatures of 290 K, 320 K (from Section 4.1), and 360 K. The pore volume to breakthrough (PVBT) values corresponding to these cases are 10.92, 6.39, and 3.12, respectively. The results indicate a strong dependence of acidizing efficiency on the injected acid temperature. As the injection temperature increases, the PVBT significantly decreases, implying faster breakthrough and more efficient acid propagation through the matrix. This trend is attributed to the temperature dependence of the reaction kinetics—higher injection temperatures accelerate the acid–rock reaction rate, leading to faster porosity development, more rapid wormhole formation, and consequently earlier breakthrough.

Formatted: Font color: Red

Figure 7 and Figure 8 present the porosity and saturation profiles at breakthrough for acid injection temperatures of 290 K and 360 K. At 360 K, dissolution is highly localized and concentrated, forming a well-developed wormhole structure. In contrast, the 290 K case exhibits a more diffuse and widespread dissolution front, indicative of slower reaction kinetics and reduced channeling efficiency. This behavior corresponds to a uniform dissolution pattern, where acid interacts more evenly with the porous matrix rather than focusing along a dominant path. The corresponding saturation profiles further support this distinction. At 360 K, water displacement is strongly aligned with the main flow path, producing a narrow and well-defined saturation front. Conversely, the 290 K case shows a broader and more dispersed water front, reflecting the less focused nature of fluid transport under cooler acid injection conditions. For the intermediate case of 320 K (as discussed in Section 4.1), the porosity profile lies between the 290 K and 360 K cases. It displays several small branching fingers extending from the injection boundary, characteristic of a ramified dissolution pattern. According to (Wu, 2015), acidizing can produce five primary dissolution patterns—face, conical, wormhole, ramified, and uniform—depending primarily on the increase of the injection velocity, assuming other conditions remain constant. Interestingly, the observed trend suggests that increasing the injected acid temperature produces similar effects to decreasing the injection velocity, both leading to a transition from uniform toward wormhole-type dissolution. This highlights the dual role of thermal and hydrodynamic controls

Deleted: Figure 4

Deleted: Figure 5

in shaping the acidizing outcome and suggests that temperature can be used as an alternative lever to optimize dissolution behavior in two-phase systems.

The acid concentration fields (Figure 9) further support these findings. At lower acid temperatures, acid is consumed more gradually and over a broader region, resulting in a more uniform concentration distribution. At 360 K, acid is rapidly consumed along the high-permeability wormhole, leading to a sharp depletion front and improved reactant utilization efficiency. The streamline patterns (Figure 10 and Figure 11) also reflect the temperature-dependent channelization behavior. For the higher acid temperature (360 K), streamlines are strongly aligned with the wormhole path, concentrating both water and oil flow into narrow regions. This results in more focused displacement and enhanced acid penetration. At 290 K, streamlines are more dispersed, suggesting a less efficient fluid transport and weaker coupling between dissolution and flow. Finally, temperature profiles (Figure 12) illustrate how injected acid influences the thermal distribution in the matrix. At 360 K, the elevated injection temperature maintains a thermal gradient that sustains high reaction rates along the main channel. In contrast, the 290 K injection case shows a cooler and more diffused thermal field, contributing to lower reaction intensity. It is noted that the temperature scales are different for the two cases in Figure 12. If a unified temperature scale is given, the change of the temperature cannot be identified clearly.

Deleted: Figure 6

Deleted: Figure 7

Deleted: Figure 8

Deleted: Figure 9

Deleted: Figure 9

In summary, the simulation results clearly demonstrate that the injected acid temperature plays a critical role in the efficiency of the acidizing process. Higher injection temperatures lead to accelerated reaction rates, more pronounced wormhole formation, and reduced PVBT values, indicating more efficient usage of the injected fluid. This finding highlights the importance of thermal management in designing effective acidizing strategies in two-phase flow systems.

4.4 Additional parametric study

Deleted: Verification experiments

As discussed above, increasing the injected acid temperature appears to have an effect analogous to decreasing the injection velocity, particularly in terms of dissolution pattern and breakthrough behavior. To further examine this relationship, two additional simulations are conducted with varying injection velocities. In all previous experiments, the injection velocity was fixed at 4.17×10^{-5} m/s. In the new cases, the injection velocity is increased to 4.17×10^{-4} m/s and 1.0×10^{-3} m/s, respectively. The injected acid temperature is maintained at 360 K, and the initial matrix temperature remains at 420 K for all scenarios. Thus, under the fixed thermal conditions, three different injection velocities are considered: 4.17×10^{-5} m/s, 4.17×10^{-4} m/s, and 1.0×10^{-3} m/s. To keep numerical stability, the simulation time steps are decreased to 0.5 second and 0.1 second for the injection velocities of 4.17×10^{-4} m/s and 1.0×10^{-3} m/s, respectively. The simulation results corresponding to the lowest velocity have already been presented in Section 4.2. The results for the two higher-velocity cases are provided and discussed in the following section.

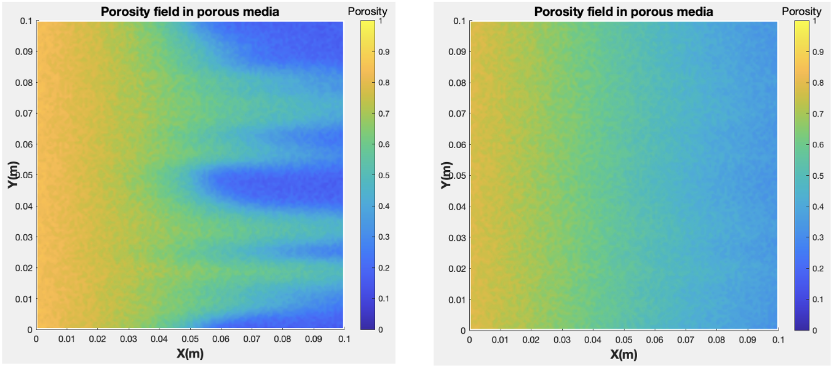

(a) Porosity profile with injection velocity of 4.17 × 10^{-4} m/s.

(b) Porosity profile with injection velocity of 1.0 × 10^{-3} m/s.

Figure 13 Porosity profiles of the two-phase experiments at breakthrough with different injection velocity.

Deleted: 10

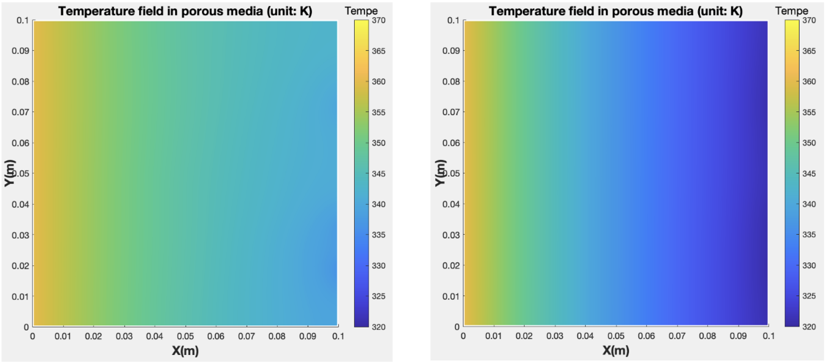

(a) Temperature profile with injection velocity of 4.17 × 10^{-4} m/s.

(b) Temperature profile with injection velocity of 1.0 × 10^{-3} m/s.

Figure 14 Temperature profiles of the two-phase experiments at breakthrough with different injection velocity.

Deleted: 11

The porosity fields at breakthrough (Figure 13) reveal a distinct shift in the dissolution pattern as the injection velocity increases. At an injection velocity of 4.17 × 10^{-4} m/s, the dissolution exhibits a ramified pattern, characterized by multiple branching wormholes extending from the injection boundary. This morphology reflects a moderately efficient reaction front where several channels compete and develop simultaneously. In contrast, at the higher injection velocity of 1.0 × 10^{-3} m/s, the dissolution becomes more uniform, with acid spreading broadly across the domain and minimal evidence of localized channeling. This suggests that the elevated flow rate dilutes the acid–rock interaction front, preventing the formation of focused wormholes and instead promoting a diffuse dissolution regime. These observed transitions align well with the established classification of dissolution patterns (face → conical → wormhole → ramified → uniform) as a function of increasing injection velocity (Wu, 2015). Specifically, the simulation with 4.17 × 10^{-4} m/s corresponds to the ramified regime, while the simulation with 1.0 × 10^{-3} m/s corresponds to the uniform regime. These

Deleted: Figure 10

findings reinforce the earlier conclusion that increasing the injected acid temperature has an effect analogous to decreasing the injection velocity, as both strategies favor more localized dissolution and efficient wormhole formation. The observations are summarized in Table 2. The temperature fields (Figure 14) show that in both cases, the matrix is thermally dominated by the injected acid at 360 K, which progressively displaces the initially hotter matrix temperature of 420 K. The primary distinction lies in the temperature gradient: the simulation with 1.0×10^{-3} m/s exhibits a wider range between the maximum and minimum temperatures, indicating a more pronounced temperature gradient. This suggests that higher injection velocities enhance advective heat transport, leading to sharper thermal fronts across the domain.

Deleted: Table 2

Deleted: Figure 11

Table 2 Dissolution patterns in different thermal and hydrodynamic conditions

Dissolution pattern	$T_{\text{injection acid}} = 360$ K $T_{\text{initial matrix}} = 420$ K	$v_{\text{injection acid}} = 4.17 \times 10^{-5}$ m/s $T_{\text{initial matrix}} = 420$ K
Uniform	$v_{\text{injection acid}} = 1.0 \times 10^{-3}$ m/s	$T_{\text{injection acid}} = 290$ K
Ramified	$v_{\text{injection acid}} = 4.17 \times 10^{-4}$ m/s	$T_{\text{injection acid}} = 320$ K
Wormhole	$v_{\text{injection acid}} = 4.17 \times 10^{-5}$ m/s	$T_{\text{injection acid}} = 360$ K

Overall, the results demonstrate that increasing the injection velocity leads to a transition from wormhole-like to ramified and eventually uniform dissolution patterns. This behavior confirms the earlier observation that raising acid temperature produces similar physical effects to lowering injection velocity, as both alter the balance between reaction and transport processes. These insights are critical for optimizing acidizing strategies, highlighting the importance of simultaneously managing temperature and flow rate to achieve the desired dissolution morphology and stimulation efficiency.

5. Conclusion and Future Work

In this work, we developed a novel two-phase thermal Darcy–Brinkman–Forchheimer (DBF) model to simulate matrix acidization processes in porous media under realistic reservoir conditions. The model integrates multiphase flow, reactive transport, heat transfer, and dynamic porosity evolution into a unified framework. Key contributions include the incorporation of temperature-dependent reaction kinetics via Arrhenius-type relationships, as well as a fully coupled numerical solution strategy that accounts for viscous, inertial, and thermal effects.

Numerical experiments were conducted to investigate the influence of initial matrix temperature, injected acid temperature, and injection velocity on the acidizing process. Results showed that the initial matrix temperature has minimal impact on wormhole formation and breakthrough behavior due to rapid thermal equilibration driven by acid injection. In contrast, the injected acid temperature significantly affects the dissolution pattern, reaction rate, and acid utilization efficiency. Higher injection temperatures enhance reaction rates and promote localized wormhole formation, resulting in earlier breakthrough and reduced pore volume to breakthrough (PVBT).

Furthermore, the simulations from additional parametric study demonstrated that increasing acid temperature has a similar effect to decreasing injection velocity. Both approaches shift the dissolution regime from uniform to wormhole-dominated patterns, highlighting a fundamental coupling between thermal and hydrodynamic controls. These insights offer practical guidance for optimizing acidizing strategies by balancing thermal input and flow rate to improve treatment efficiency and control wormhole geometry.

Deleted: verification

Deleted: ¶

The present work primarily serves as a methodological study for investigating coupled thermo-hydraulic-reactive processes in two-phase thermal acidizing systems. Although the proposed framework demonstrates the capability to capture the influence of thermal and hydrodynamic conditions on dissolution behavior and wormhole formation in laboratory-scale simulations, several aspects require further investigation before broader practical applications can be considered.

Future work will focus on extending the current framework to more complex porous media configurations, including heterogeneous permeability and porosity distributions, natural fractures, and vuggy carbonate structures. In addition, incorporating multi-mineral reaction mechanisms and competing acid–rock interactions may improve the representation of chemically complex reservoir conditions. Since the present study is limited to two-dimensional laboratory-scale numerical experiments, additional work is also required to investigate larger-scale simulations and improve computational efficiency through techniques such as parallel computing optimization and adaptive mesh refinement.

Furthermore, validation against experimental observations and established benchmark studies will be an important direction for future research in order to further assess the predictive capability and robustness of the proposed model. Possible future extensions may also include coupling with wellbore and reservoir-scale models, as well as the development of reduced-order or surrogate models for efficient parameter studies and optimization tasks.

Deleted: While the current model provides a robust platform for simulating two-phase thermal acidizing, several directions remain for further enhancement. Future extensions will incorporate complex geological features such as natural fractures, vugs, and spatial heterogeneity in porosity and permeability. These additions will enable more realistic simulation of carbonate formations and fractured reservoirs. Moreover, the current study focuses on lab-scale domains. Scaling up the framework to field-scale models will require further optimization of the numerical solver, including parallel performance tuning and adaptive mesh refinement techniques. Besides that, incorporating multi-mineral reaction kinetics and competing acid–rock interactions (e.g., dolomite and calcite dissolution) will enhance the chemical fidelity of the model and broaden its applicability to various rock types. To better evaluate stimulation effectiveness, coupling the matrix acidizing model with wellbore dynamics and reservoir-scale production forecasting will be explored. Furthermore, data from high-fidelity simulations can be used to train surrogate models or integrate with machine learning algorithms for real-time optimization of injection schedules, temperature control, and acid composition.¶
These directions will further strengthen the capability of the proposed framework for practical reservoir engineering applications and enable more accurate design and evaluation of acidizing treatments in complex subsurface environments.¶

Code availability

Name of the code: Two-phase thermal DBF matrix acidizing simulator
Contact: wuyuanq@gmail.com, +86-13928772190
Hardware requirements: CPU: 2.2 GHz 6-Core Intel Core i7, Memory: 16 GB 2400 MHz DDR4
Program language: FORTRAN90, MATLAB, TECPLOT
Software required: LAPACK, UMFPACK, MUMPS, HYPRE, MPI
Program size: more than 10000 lines
The source codes are available for downloading at the link: https://doi.org/10.5281/zenodo.17272888 (Wu, 2025)

Author contribution

Wu: programming, the design and realization of the numerical experiments, the writing of the work. Kou: concepts of the work, the development of the numerical models, the algorithm design of the numerical scheme, the writing of the work.

Competing interests

The authors declare that they have no conflict of interest.

Acknowledgements

This manuscript was prepared with the assistance of ChatGPT, a language model developed by OpenAI, which was used for refining language. The authors have reviewed, revised and approved the final content.

References

Alokaily, S. A.: Numerical Simulations of Fluid Transport in Heterogeneous Darcy–Forchheimer–Brinkman Layers, Journal of Fluids Engineering, 144(12), 121404, https://doi.org/10.1115/1.4055072, 2022.

Araújo, E. D. A., Schwalbert, M. P., Leitão, R. J., & Aum, P. T. P.: Influence of Matrix-Acidizing Design on Oil Recovery and Economics in Carbonate Reservoirs Undergoing Waterflooding Offshore in Brazil, Energies, 17(4), 883, https://doi.org/10.3390/en17040883, 2024.

Babaei, M., & Sedighi, M.: Impact of phase saturation on wormhole formation in rock matrix acidizing, Chemical Engineering Science, 177, 39-52, https://doi.org/10.1016/j.ces.2017.10.046, 2018.

Daccord, G., Lenormand, R., & Lietard, O.: Chemical dissolution of a porous medium by a reactive fluid—I. Model for the “wormholing” phenomenon, Chemical Engineering Science, 48(1), 169-178, https://doi.org/10.1016/0009-2509(93)80293-Y, 1993. a

Daccord, G., Lietard, O., & Lenormand, R.: Chemical dissolution of a porous medium by a reactive fluid—II. Convection vs reaction, behavior diagram, Chemical engineering science, 48(1), 179-186, https://doi.org/10.1016/0009-2509(93)80294-Z, 1993. b

Deb, N., Farshi, M. S., Das, P. K., & Saha, S.: Convective flow optimization inside a lid-driven chamber with a rotating porous cylinder using Darcy–Brinkman–Forchheimer model, Journal of Thermal Analysis and Calorimetry, 149(12), 6125-6146, https://doi.org/10.1007/s10973-024-13228-y, 2024.

Elsafih, M., & Fahes, M.: Quantifying the effect of multiphase flow on matrix acidizing in oil-Bearing carbonate formations, SPE Production & Operations, 36(04), 795-806, https://doi.org/10.2118/205397-PA, 2021.

Fredd, C. N., & Fogler, H. S.: Influence of transport and reaction on wormhole formation in porous media, AIChE journal, 44(9), 1933-1949, https://doi.org/10.1002/aic.690440902, 1998.

Golfier, F., Zarcone, C., Bazin, B., Lenormand, R., Lasseux, D., & Quintard, M.: On the ability of a Darcy-scale model to capture wormhole formation during the dissolution of a porous medium, Journal of fluid Mechanics, 457, 213-254, https://doi.org/10.1017/S0022112002007735, 2002.

Jia, C., Sepehrnoori, K., & Yao, J.: Numerical studies and analysis on reactive flow in matrix acidizing coupled thermal-hydrological-mechanical-chemical processes, In ARMA US Rock Mechanics/Geomechanics Symposium (pp. ARMA-2021). ARMA, 2021 June.

Kou, J., Sun, S., & Wu, Y.: Mixed finite element-based fully conservative methods for simulating wormhole propagation, Computer Methods in Applied Mechanics and Engineering, 298, 279-302, https://doi.org/10.1016/j.cma.2015.09.015, 2016.

Kou, J., Sun, S., & Wu, Y.: A semi-analytic porosity evolution scheme for simulating wormhole propagation with the Darcy–Brinkman–Forchheimer model, Journal of Computational and Applied Mathematics, 348, 401-420, https://doi.org/10.1016/j.cam.2018.08.055, 2019.

Kou, J., Du, S., & Zhong, Z.: Energy stable modeling of two-phase flow in porous media with fluid–fluid friction force using a Maxwell-Stefan-Darcy approach, Physics of Fluids, 33, 073312, https://doi.org/10.1063/5.0053373, 2021.

Kou, J., Chen, H., Du, S., & Sun, S.: An efficient and physically consistent numerical method for the Maxwell-Stefan-Darcy model of two-phase flow in porous media, International Journal for Numerical Methods in Engineering, 124(3), 546-569, https://doi.org/10.1002/nme.7131, 2023.

Kou, J., Wang, X.: Numerical modeling of unsaturated flow in porous media using a thermodynamical approach, Capillarity, 11, 63-69, https://doi.org/10.46690/capi.2024.06.01, 2024.

Ma, G., Chen, Y., Wang, H., Li, T., & Nie, W.: Numerical analysis of two-phase acidizing in fractured carbonate rocks, Journal of Natural Gas Science and Engineering, 103, 104616, https://doi.org/10.1016/j.jngse.2022.104616, 2022.

Mahdavi Kalatehno, J., Khamehchi, E., Keihanikamal, M., Yousefmarzi, F., Dargi, M., & Daneshfar, P.: A successful case study of using HCl and viscoelastic diverting acid systems for carbonate matrix acidizing in an oil well with optimized predictive model, Journal of Petroleum Exploration and Production Technology, 15(1), 1, https://doi.org/10.1007/s13202-024-01896-3, 2025.

Panga, M. K., Ziauddin, M., & Balakotaiah, V.: Two - scale continuum model for simulation of wormholes in carbonate acidization, AIChE journal, 51(12), 3231-3248, https://doi.org/10.1002/aic.10574, 2005.

Qureshi, U., Qureshi, H. A., Bhatti, A. A., Saeed, M. S., & Khalid, M. S.: Investigating the effects of matrix acidizing and acid fracturing on the production optimization of a carbonate reservoir: a case study, Arabian Journal of Geosciences, 16(11), 620, https://doi.org/10.1007/s12517-023-11734-1, 2023.

Sabooniha, E., Rokhforouz, M. R., Kazemi, A., & Ayatollahi, S.: Numerical analysis of two-phase flow in heterogeneous porous media during pre-flush stage of matrix acidizing: Optimization by response surface methodology, Physics of Fluids, 33(5), https://doi.org/10.1063/5.0046106, 2021.

Shahid, A., Wei, W., Abbas, T., & Bhatti, M. M.: A computational investigation of diffusivities and heat transfer in the flow of viscoelastic fluid through Darcy–Brinkman–Forchheimer medium, Numerical Heat Transfer, Part B: Fundamentals, 86(3), 762-779, https://doi.org/10.1080/10407790.2023.2296076, 2025.

Wei, W., Varavei, A., & Sepehrnoori, K.: Modeling and analysis on the effect of two-phase flow on wormhole propagation in carbonate acidizing, SPE Journal, 22(06), 2067-2083, https://doi.org/10.2118/186111-pa, 2017.

Wu, Y.: Parallel reservoir simulations with sparse grid techniques and applications to wormhole propagation, 2015.

Wu, Y. (2025). Two-phase thermal DBF matrix acidizing simulator. Zenodo. https://doi.org/10.5281/zenodo.17272888

Wu, Y., Kou, J., & Sun, S.: Matrix acidization in fractured porous media with the continuum fracture model and thermal Darcy-Brinkman-Forchheimer framework, Journal of Petroleum Science and Engineering, 211, 110210, https://doi.org/10.1016/j.petrol.2022.110210, 2022.

Wu, Y., Kou, J., Sun, S., & Wu, Y. S.: Thermodynamically consistent Darcy–Brinkman–Forchheimer framework in matrix acidization, Oil & Gas Science and Technology–Revue d'IFP Energies nouvelles, 76, 8, https://doi.org/10.2516/ogst/2020091, 2021.

Wu, Y., Salama, A., & Sun, S.: Parallel simulation of wormhole propagation with the Darcy–Brinkman–Forchheimer framework, Computers and Geotechnics, 69, 564-577, https://doi.org/10.1016/j.compgeo.2015.06.021, 2015.

Wu, Y., & Ye, M.: A Newton's second law abided Darcy-Brinkman-Forchheimer framework in matrix acidization simulation, In International Conference on Computational & Experimental Engineering and Sciences (pp. 861-866), Cham: Springer International Publishing, https://doi.org/10.1007/978-3-030-27053-7_73, 2019 March.

Yoon, H. C., & Mallikarjunaiah, S. M.: A stabilized finite element method for steady Darcy-Brinkman-Forchheimer flow model with different viscous and inertial resistances in porous media, arXiv preprint arXiv:2501.04041, 2025.

Zhou, L., Guo, A., Wang, X., Qiao, J., & Tang, X.: The effect of temperature, natural fractures and vugs on the acidizing process in fractured-vuggy reservoirs with hydro-thermal-chemical coupled modeling, Journal of Petroleum Science and Engineering, 213, 110416, https://doi.org/10.1016/j.petrol.2022.110416, 2022.